Regular Article

ANALYTICAL
AND BIOANALYTICAL
CHEMISTRY
RESEARCH

Published by the
Iranian Chemical Society

***Anal. Bioanal. Chem. Res.**, Vol. 10, No. 1, 45-62, January 2023.*

Removal of Direct Red 23 Dye Using $CeO_2/NiO/NiAl_2O_4$ Nanocomposite: Mechanism, Kinetic, Thermodynamic, and Equilibrium Studies

Marziyeh Saati[a], Samin Hamidi[b,c,*], Naeimeh Jarolmasjed[a], Zolfaghar Rezvani[d] and Soheila Davari[e]

[a]*Department of Chemistry, Payame Noor University, P. O. Box: 19395-3697 Tehran, Iran*

[b]*Food and Drug Safety Research Center, Tabriz University of Medical Sciences, Tabriz, Iran*

[c]*Pharmaceutical Analysis Research Center, Tabriz University of Medical Sciences, Tabriz, Iran*

[d]*Department of Chemistry, Faculty of Basic Sciences, Azarbaijan Shahid Madani University, Tabriz, Iran*

[e]*Tabriz Hadi Wire & Cable Co, Tabriz, Iran*

(Received 27 June 2022, Accepted 11 September 2022)

We designed a facial and novel $CeO_2/NiO/NiAl_2O_4$ nanocomposite prepared by recalcination of the cerium impregnated product of the primary calcined production of NiAl-NO_3 layered double hydroxide (LDH) through the structural memory effect. The materialization of as-prepared nanocomposite was confirmed by Fourier-transform infrared (FT-IR) spectroscopy, powder X-ray diffraction (XRD), scanning electron microscopy (SEM), thermal gravimetry (TG), dynamic light scattering (DLS) and transmission electron microscopy (TEM). Morphologic studies revealed that the size of the nanocomposite was below 100 nm. The resulting mixed metal oxide nanocomposite was employed as an efficient adsorbent for the removal of Direct Red 23 (DR23) as a model pollutant from textile wastewater. The dye removal study showed >98% efficiency for the removal of dye which revealed the superiority of material for decontamination of waste water, while the maximum adsorption capacity determined from isotherm data was 588.24 mg of dye per g of the adsorbent. In addition, the reusability was also performed up to three cycles with 89, 85 and 88% efficiency for DR23. Also, thermodynamics, isotherm and kinetic studies were investigated. Overall, we offer a facile method for synthesizing $CeO_2/NiO/NiAl_2O_4$ nanocomposite, efficiently decontaminating DR23 from water with good recyclability.

Keywords: $CeO_2/NiO/NiAl_2O_4$ nanocomposite, Dye removal, Isotherm studies, Water safety

INTRODUCTION

The discharge of industrial wastes and groundwater contamination has recently drastically exposed the environment, human health, and aquatic life to severe problems due to their toxic effects and carcinogenic properties [1-4]. As a result, several studies have been devoted to finding an effective solution for purifying dye-containing wastewater [5]. Azo dyes are one of the most important synthetic dyes. Azo dyes are structurally composed of (-N=N-) groups attached to aromatic groups, like naphthalene or benzene, by sp^2 hybrid carbon atoms [6,7]. These compounds are very polar and soluble in water because of the sulfonate groups in their structure [8]. If these azo compounds enter the body, they are broken down by liver enzymes into their constituent compounds, including aromatics that can cause carcinogenic signals when ingested [9,10]. Azo compounds have a firm, stable, and complex structure, proving their resistance to many chemical and photochemical degradations and eliminations. Efforts to find inexpensive adsorbents that can remove paint with high adsorption capacity and kinetics are of great interest [11].

*Corresponding author. E-mail: Hamidisamin@gmail.com

Direct Red 23 (DR23) is a very toxic and carcinogenic dye among the various synthetic dyes. Moreover, its complex and stable chemical structure does not decompose in the environment [12]. DR23 is a red-purple powder containing azo group, a water-soluble dye that gives the solution a red color. This dye is widely used in textile industries, with cotton fabrics dyeing at near boiling temperatures. In addition, it is highly employed in leather, silk, wool, paper, and pulp dyeing.

Unfortunately, due to its incomplete use in the coloring process and washing operations, it is continuously released into the environment, causing severe health-related problems [13]. Hence, its removal from the water streams of textile, cosmetics, and paper industries' colored effluents is necessary.

Various methods are developed to remove hazardous materials from industrial wastewater, such as coagulation, precipitation, membrane filtration, electrochemical methods, photodegradation, Fenton reagent, and ozone process [14, 15]. However, the chemical and biological processes are not cost-effective in wastewater treatment processes; thus, supplementary chemical reactions are needed to eliminate the sludge containing fully complex chemicals (such as aromatic amines) at the end of operations [16].

In contrast, physical processes can effectively translocate dye molecules without destroying their structure. Furthermore, they are especially suitable when the amount of effluent is low. Therefore, adsorption methods for effective performance, ease of availability, low cost, operation flexibility, and convenience could be superior to other methods. This advantage is despite the cost and time-consuming regenerated process, which usually accompanies the adsorbents [17].

Various adsorbents were introduced for removing dye from contaminated water, including activated carbon [18, 19], sepiolite [20], vermiculite [21], and carbon nanotube [22,23]. Layered double hydroxides (LDHs) are two-dimensional materials made up of a brucite-like structure with a general formula of $[M^{2+}_{1-x}M'^{3+}_{x}(OH)_2]^{x+}(A^{n-}_{x/n}).mH_2O$. In this formula, M^{2+} and M'^{3+} can be di- and trivalent metal ions like Fe^{2+}, Co^{2+}, Cu^{2+}, Ni^{2+}, Al^{3+}, Cr^{3+}, In^{3+}, Mn^{3+} which occupy octahedral holes of hydroxyl ions. The anions (A^{n-}) such as CO_3^{2}, SO_4^{2-}, OH^-, NO_3^-, and halogen anions are placed between the layers for charge neutrality, resulting in

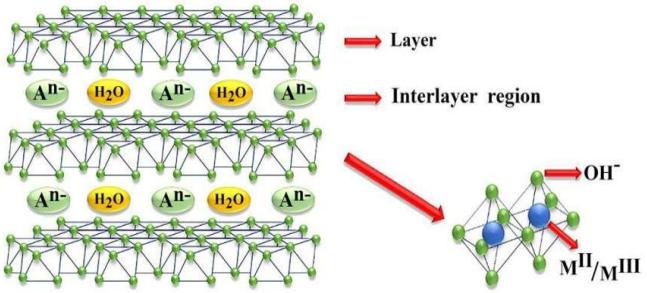

Fig. 1. Structure of a typical Layered Double Hydroxide (LDH).

LDHs with m numbers of H_2O molecules in the lamellar structure [24]. The structure of a typical LDH is presented in Fig. 1.

In addition, LDHs have some characteristic virtues, such as high surface area, thermal stability, and memory effect, which shows that the calcined product can be regenerated by rehydration [25]. In addition, LDHs are easily synthesized, and non-toxic materials are used to prepare them, which avoids harming the environment [26]. Furthermore, LDHs and the calcined multi-metal oxide products effectively remove floating or water-soluble contaminants at a low cost [27-30].

Besides, CeO_2 is one of the rare earth metal oxides widely utilized in catalysis, electrochemistry, optical applications, and as an adsorbent [31-33]. However, utilizing CeO_2 as a single functional material suffers from several drawbacks. For example, pure CeO_2 is a poor thermo-stable material and undergoes rapid sintering at high temperatures [34]. Additionally, LDHs, due to their versatility, can be proper support for ceria. In addition, CeO_2-impregnated LDH presents outstanding thermal and chemical stability and may offer a new stable compound.

To efficiently remove DR23 from water samples, the present work aimed to synthesize CeO_2-NiAl-NO_3 LDH and the derived mixed metal oxides. This study was the first report on using $CeO_2/NiO/NiAl_2O_4$ as an adsorbent to remove the dye. In addition, different techniques, such as XRD, FT-IR, and TG analysis, were used to confirm the nanocomposite structure. The adsorption mechanism to know the isotherm and kinetic trends of the nanocomposite were also evaluated. Moreover, the influential factors on the adsorption process of a dye, such as a contact time, pH, and

temperature, were examined in detail to get the optimized multiple variables.

EXPERIMENTAL

Materials

Nickel(II) nitrate hexahydrate ($Ni(NO_3)_2.6H_2O$), aluminum nitrate nonahydrate ($Al(NO_3)_3.9H_2O$), cerium(III) nitrate hexahydrate ($Ce(NO_3)_3.6H_2O$), DR23 (30%) and other materials were purchased from Sigma-Aldrich. Due to the presence of CO_2 gas in the air and the fact that it can form carbonate in combination with water and enter the nanocomposite layers, deionized water is boiled before use and saturated with nitrogen gas [31]. The characteristics of DR23 dye are detailed in Table 2.

LDH Synthesis Method

The conventional co-precipitation method synthesized LDH containing Ni^{2+} and Al^{3+} with the cationic ratio of 2 at fixed pH [32]. The economical and straightforward synthetic procedure reported by Olanrewaju *et al.* and Li *et al.* was used to synthesize NiAl-NO_3 LDH under ambient pressure. Briefly, to prepare 1 g of LDH, 0.870 g (0.003 mol) of $Ni(NO_3)_2.6H_2O$ and 0.375 g (0.001 mol) of $Al(NO_3)_3.9H_2O$ were added into 17 ml of deionized water. After completely dissolving the salts, the NaOH (1 M) solution was poured drop by drop into the solution of Ni^{2+} and Al^{3+} and well mixed until the pH value became constant. After the salts were dissolved in water by sodium hydroxide 1 M, the resulting mixture was placed under nitrogen gas for half an hour to avoid the entry of CO_2 gas. A polypropylene vessel was used in this experiment [33]. The pH value was followed continuously until it reached 6 [34]. Then, the mixture was transferred to an oven for 24 h at 180 °C. The solid residue was separated by centrifuge, washed with deionized water (3 times), and dried at 70 °C for 4 h.

Cerium Impregnation Method

Coating the surface of the as-prepared NiAl-NO_3 LDH with CeO_2 nanoparticles was performed in CO_2-free deionized water in the presence of desired ions. The NiAl-NO_3 LDH (1 g) was pulverized and calcined at 500 °C for 5 h (ramp: 5 °C min^{-1}). The calcined solid was then suspended in 10 ml of $Ce(NO_3)_3.6H_2O$ (0.5 M) solution and aged at 100 °C for 5 h under continuous fast stirring conditions [35]. By obtaining a homogeneous gel, the LDH structure was wholly reconstructed with pH 9. Finally, the sample was filtered and washed with double distilled water three times, dried at 60 °C overnight, and denoted as CeO_2/NiAl-NO_3 LDH. After calcination at 900 °C for 3 h (ramp: 5 °C min^{-1}), the mixed metal oxide material was marked as CeO_2/NiO/$NiAl_2O_4$ nanocomposite.

Regeneration Experiment

The dye-saturated nanocomposite obtained from the adsorption process was poured into an alkaline solution (pH = 8) while stirring at room temperature for 2 h. The regenerated nanocomposite was re-entered in the adsorption process.

Characterizations

The Fourier transform infrared (FT-IR) spectra of the as-prepared samples were analyzed in 400-4000 cm^{-1} by Shimadzu 8400s spectrometer using KBr pressed disks (samples to dry KBr were 0.1: 400 mg) at room temperature. The powder X-ray diffraction (XRD) patterns of the prepared solids were obtained by a Bruker D8 Advance type X-ray diffractometer using $Cu - K_\alpha$ radiation (λ = 1.542 Å) at room temperature with a Bragg angle of 5-70° at a 5° min^{-1} scan speed. The thermogravimetric (TG) analysis was recorded on

Table 2. Characteristics of Direct Red 23

Chemical structure	Classification	Chemical type	Color index	λ_{max} (nm)	Mw (g mol^{-1})
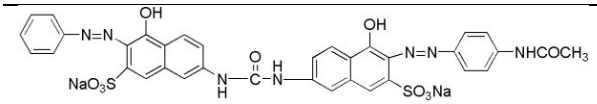	Anionic	Diazo	29160	505	813.7
$C_{35}H_{25}N_7Na_2O_{10}S_2$					

a Mettler-Toledo TGA 851e apparatus at a heating rate of 10 °C min^{-1} and argon flow of 20 ml min^{-1}. The UV-Vis absorption spectra were performed on a Shimadzu UV-1601 PC instrument in 200-800 nm. A calibration curve was plotted to correlate the analytical responses with the dye concentrations. Scanning electron microscopy (SEM) image was recorded using Hitachi S 4160 model scanning microscope. Transmission electron microscopy (TEM) was used on a Hitachi H99 transmission electron microscope operating at an accelerating voltage of 100 kV to elucidate the morphology of nanocomposites. The synthesized powder sample was fully dispersed in distilled water, ultrasonically homogenized, and deposited on an aluminum film for SEM analysis. The powdered samples were dispersed in ethanol, and one drop was put on a TEM micro-grid. The dynamic light scattering (DLS) diameter of LDHs was measured using photon correlation spectroscopy (PCS, Nanosizer Nano ZS, Malvern Instruments).

Batch Adsorption Studies

To prepare the dye stock solution, 1000 mg of pure DR23 was poured into deionized water, and then the resulting solution was brought to a volume of 1000 ml. 24 mg l^{-1} solutions of DR23 were prepared at pH = 12, 10, 8, 6, and 4, and buffer was used to adjust and keep the pH constant. To prepare 100 ml of solution with pH 4, phosphate buffer solution was used. To prepare the buffer, 1.021 g (0.177 mol) of potassium hydrogen phosphate plus 0.1 ml of 0.1 M hydrochloric acid dissolved in deionized water and then the volume of the solution reach to 100 ml. The number recorded for pH by the pH meter was 4. To prepare solutions with pH 6 and 8, the preparation method is similar to that for pH 4, with the difference that for the solution with pH 6, from 0.681 g (0.092 mol) of potassium dihydrogen phosphate plus 5.6 mL of sodium hydroxide 0.1 M and for the solution with pH 8, 0.681 g (0.092 mol) of potassium dihydrogen phosphate in addition to 46.7 ml of sodium hydroxide 0.1 M was used.

To prepare 100 ml of ammonia buffer solution (pH 10), 7 g (0.374 mol) of ammonium chloride and 56.8 ml of ammonia are dissolved in deionized water. Then the volume of the solution is brought to 100 ml. To be likewise, to prepare 100 ml of buffer solution (pH 12), the 5 ml of 0.2 M potassium chloride plus a specific volume of 0.2 M sodium hydroxide is combined with deionized water. The pH of the solution is set at 12.

The dye adsorption tests on the freshly synthesized nanocomposite were carried out in 3 different manners: the pH-dependent (4-12), the time-dependent (0-180 min) and the temperature-dependent (293-338 K) adsorption. A thermostatic container was used to record the adsorption equilibrium experiments in the batch-type equilibration method. A tightly closed and somehow isolated vessel with a fixed temperature was used to perform the experiments to prevent water evaporation. Three concentrations of 10, 20, and 30 mg of nanocomposite were tested and corresponding removal percentages were 10.30, 57.53, and 73.86%, respectively and finally, 30 mg was selected as the optimum amount for dye removal. The experiments were done by placing the containers filled with 100 ml solution of 24 mg l^{-1} of DR23 in an oil bath and maintained at desired temperatures (293-338 K). After equilibrating (time of 180 min and temperature 338 K), 30 mg of adsorbent at pH 4 and was put into the vessels. The solutions were magnetically stirred in darkness with a speed rate of 100 rpm. Then, 1 ml of solution was drawn from the sample at different time intervals and centrifuged and DR23 concentrations were determined using Shimadzu 1601-PC UV-Vis spectrophotometer at 505 nm. The initial and final concentrations subtraction indicates the dosage of DR23 absorbed by the adsorbent. All experiments were repeated three times and an error below 5% was found to be acceptable.

Removal efficiency or R% of dye was estimated by the Eq. (1), in which, C_i and C_e (mg l^{-1}) are the DR23 concentrations in the initial and at equilibrium in solution, respectively:

$$R(\%) = \frac{C_i - C_e}{C_i} \times 100 \quad (1)$$

The study of kinetic parameters was practiced at different contact times (0-180 min) at temperatures 293, 308, 323, and 338 K. The amount of DR23 per unit mass of the dry solid at time t (q_t (mg g^{-1})) was estimated using the Eq. (2):

$$q_t = \frac{(C_i - C_t) \times V}{m} \quad (2)$$

with the C_i (DR23 concentrations); C_t (mg l^{-1}) is the DR23 concentration at time t; V (l) is the volume of the dye solution; and m (g) denoted the dosage of dry adsorbent [36, 37].

The appropriate amount of adsorbent and dye mixed well and the isotherm experiments set up to know the adsorption mechanism Adsorbent capacity at the equilibrium point was calculated from the q_e *the* equation as follows and defined as mg of dye adsorbed one gram of adsorbent at equilibrium (q_e, mg g^{-1}) was calculated by the Eq. (3):

$$q_e = \frac{(C_i - C_e) \times V}{m} \quad (3)$$

Then, Freundlich and Langmuir's models were given based on data processing.

RESULTS AND DISCUSSION

Characterization of the Prepared Samples

XRD analysis. Figure 2 shows the XRD graphs of NiAl-NO_3 LDH, CeO_2-NiAl-NO_3 LDH, CeO_2/NiO/$NiAl_2O_4$ nanocomposite and DR23 adsorbed nanocomposite.

The XRD model of NiAl-NO_3 LDH, shown in Figure 2a, fits well with individual layered double hydroxide structures. Reflections at 2θ° (10.15° and 19.95° 2θ correspond to (003) and (006) basal reflections, respectively are confirmed the stacking structure of LDHs. Belonging asymmetric reflections appeared at 2θ angles of 34.75° and 61.65° and were related to the (012) and (110) non-basal reflections, respectively, with no other crystalline phases as an impurity [38]. According to the XRD pattern of Fig. 2a, the d-spacing

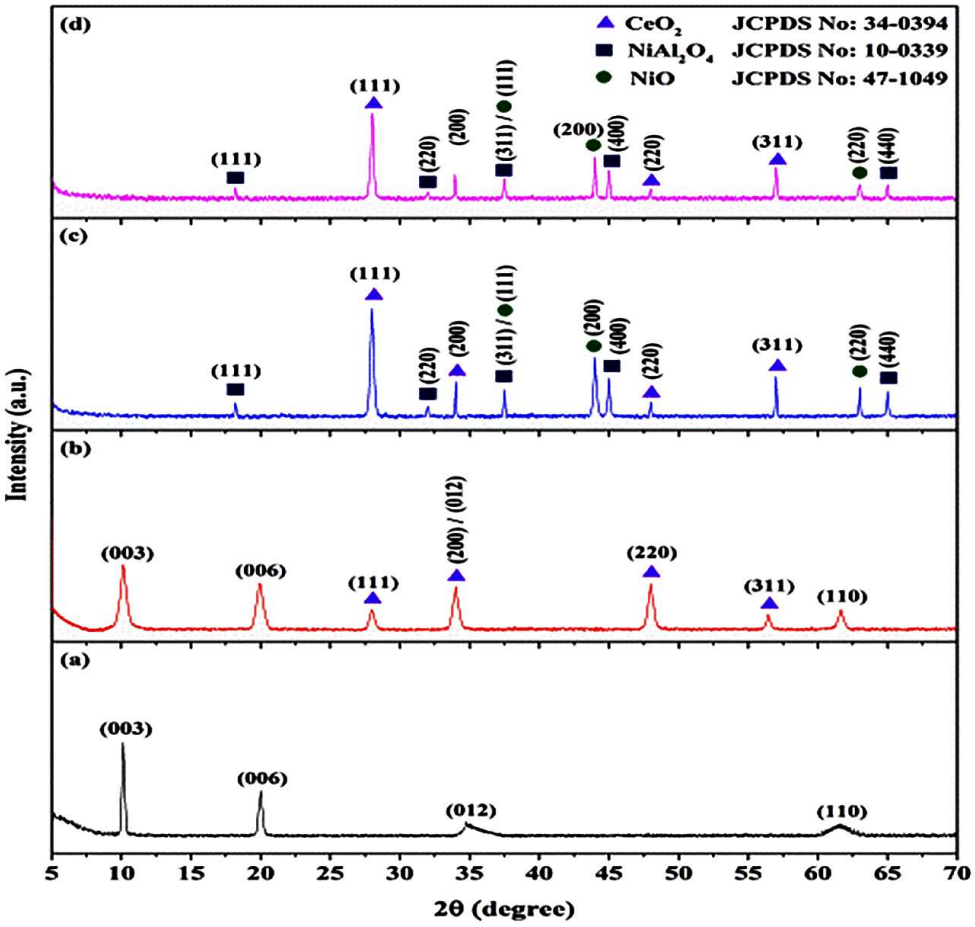

Fig. 2. The XRD patterns of: a) NiAl-NO_3 LDH; b) CeO_2-NiAl-NO_3 LDH; c) CeO_2/NiO/$NiAl_2O_4$ nanocomposite and d) DR23 adsorbed nanocomposite.

of 8.7 Å for (003) planes are assigned to nitrate from LDH [39].

The XRD pattern of reconstructed LDH in the Ce^{4+} environment depicted in Fig. 2b shows the peaks appeared at 2θ = 28°, 34° (overlapped with the LDH), 48° and 56.45° ascribed to the (111), (200), (220) and (311) reflections of CeO_2 cubic fluorite design beside as mentioned LDH characteristic peaks for NiAl-NO_3 LDH [35]. With no evidence of the presence of NiO and Ni(Al)O in the XRD pattern of the reconstructed NiAl-LDH in Ce^{4+} environment by the memory effect, it can be concluded that the layered structure is fully preserved under the wet impregnation condition. The sample recovered its original green color with a slight tendency to become dark. The LDH unit cell parameters (c and a), which correspond to the average interlayer and cation-cation distances, were calculated by 2θ degree of (003) and (110) reflections, respectively. In both parent and reconstructed LDH samples, related peaks of (003) and (110) reflections appeared at 2θ ≈ 10° and 61°, suggesting that the interlamellar distances are intercalated with NO_3^- anions. Furthermore, a cell parameter value reveals that all of the Ni^{2+} and Al^{3+} cations are engaged in the layered architecture by the memory effect reconstruction method; and cerium doesn`t penetrate the LDH lamellar structure and presents as a distinctive phase since the large ionic radius of Ce^{4+} results more considerable average cation-cation distance. So the cerium impregnation of calcined LDH will produce CeO_2-NiAl-NO_3 LDH.

The XRD pattern of the calcined product of CeO_2-NiAl-NO_3 LDH is shown in Fig. 2c. The peaks observed at 18.20°, 32°, 37.80°, 45° and 65° of 2θ corresponded to (111), (220), (311), (400) and (440) reflections, respectively, were assigned to the cubic inverse spinel $NiAl_2O_4$ phase [JCPDS No. 10-0339]. The peaks obtained in 2θ angles of 37.20° (overlapped with (311) reflection of $NiAl_2O_4$), 44° and 63° are related to (111), (200) and (220) reflections of NiO, respectively [JCPDS No. 47-1049]. In addition, the characteristic peaks at 28°, 34°, 48° and 57° were attributed to CeO_2 in nanocomposite material corresponded to its (111), (200), (220) and (311) conventional reflections, respectively [JCPDS No. 34-0394]. Consequently, the CeO_2/NiO/$NiAl_2O_4$ nanocomposite formation has been strongly confirmed [40].

The crystallite size of 43 nm for CeO_2 phase of nanocomposite was estimated from the line broadening at half the most intense peak of related (111) reflection using the Scherrer equation. In the same way, the average crystallite sizes of 55 nm for NiO and 86 nm for $NiAl_2O_4$ can be estimated from Fig. 3c using the average values of the (200), (220) and (220), (440) reflections, respectively.

Finally, the XRD pattern of DR23 adsorbed nanocomposite was shown in Fig. 2d. According to the XRD patterns, it was observed that the structure of nanocomposite was kept intact after dye adsorption with no reconstruction evidence of LDH structure. The formation of $NiAl_2O_4$ spinel phase at elevated temperature causes an irreversible change in the mixed metal oxides and hinders the reconstruction of the lamellar structure by memory effect. By the way, $NiAl_2O_4$ formation quenches the memory effect property by segregating different phases of obtained oxides [41,42].

FTIR spectra. Figure 3 depicts the FT-IR spectra of NiAl-NO_3 LDH, CeO_2-NiAl-NO_3 LDH, CeO_2/NiO/$NiAl_2O_4$ nanocomposite DR23and DR23 adsorbed on CeO_2/NiO/$NiAl_2O_4$ nanocomposite.

To eliminate the physisorbed water molecules on the surface of LDHs, they dried at 100 ° for 1 h before analysis by IR. In spectrum 3a, the broad peak at about 3500 cm^{-1} was ascribed to the stretching vibrations of -O-H groups of both the layer hydroxides and water molecules present between the layers and its broadening was ascribed to inevitable hydrogen-bonded between them and also to the slightly remained surface adsorbed water [43]. A little peak at 1630 cm^{-1} is related to the bending mode of -O-H groups [44]. The intense peak observed at 1384 cm^{-1} is attributed to the vibration frequencies of inter-lamellar NO_3^- anions. The sharp and small peak recorded at 830 cm^{-1} can be denoted as nitrate and the peak aligned at 615 cm^{-1} was assigned to OH groups. The little bands at 560 and 430 cm^{-1} can be interpreted as translational modes of AlO_6 oxygen atoms [24, 45].

The FT-IR spectrum of CeO_2-NiAl-NO_3 LDH in Fig. 3b shows the broad peak of stretching vibrations of -O-H groups centered at 3459 cm^{-1}, ascribed to both octahedrally aligned hydroxide ions around the metal cations in the hydrotalcite layers and inter-lamellar water content. The M-OH vibration and bending mode of interlayer water molecules, δ(H_2O), weak absorption band can be shown at 1627 cm^{-1}. The sharp absorption peak of NO_3^- ions vibrations aligned at 1380 cm^{-1}

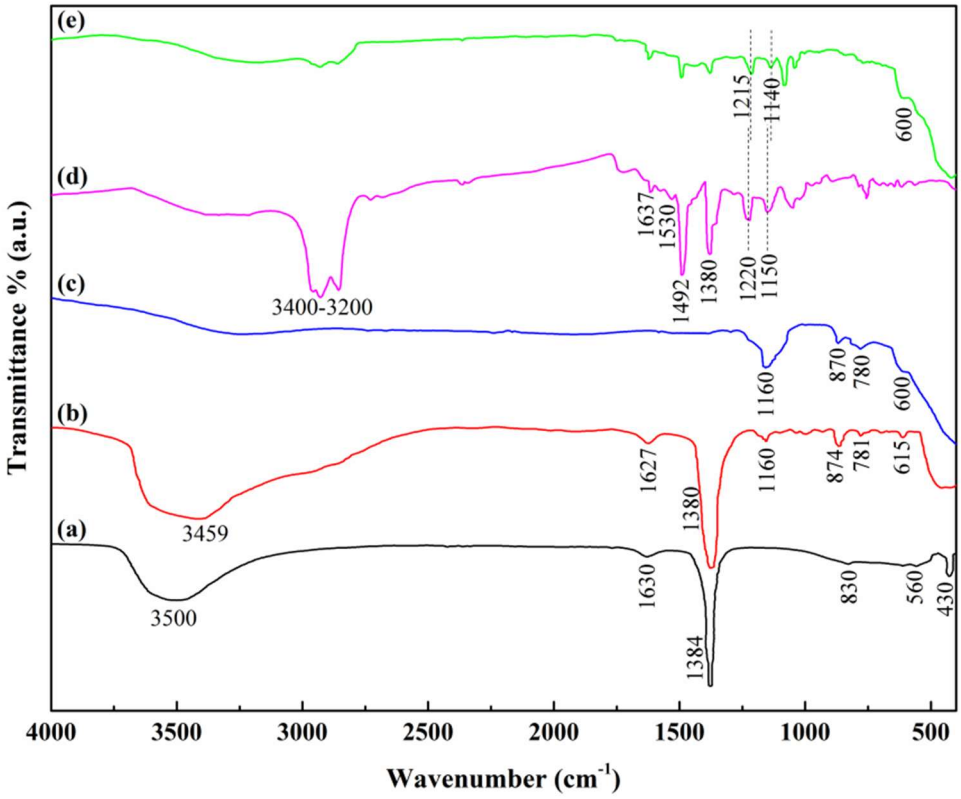

Fig. 3. The FT-IR spectra of: a) NiAl-NO_3 LDH; b) CeO_2-NiAl-NO_3 LDH; c) CeO_2/NiO/$NiAl_2O_4$ nanocomposite d) DR23 and e) DR23 adsorbed on CeO_2/NiO/$NiAl_2O_4$ nanocomposite.

is valid evidence for nitrated LDH formation by LDH memory effect. The peak of the stretching vibration of Ce-O-Ce has been aligned at 1160 cm^{-1}, accompanied by the strong and broad band of related bending vibration mode below 550 cm^{-1}. Finally, the bands at 874, 781 and 615 cm^{-1} are related to the lattice vibration modes and may be attributed to Ce-O, Al-O, and OH groups, respectively [46].

Figure 3c shows the FT-IR spectrum of CeO_2/NiO/$NiAl_2O_4$ nanocomposite. The characteristic absorption bands for stretching and bending vibrations of Ce-O-Ce bond could be seen at 1160 and below 550 cm^{-1}, respectively. Correspondingly, the weak absorption bands at 870 and 780 cm^{-1} were attributed to Ce-O and Al-O stretching vibrations. Finally, a characteristic small shoulder at 600 cm^{-1} is reasonable evidence for the $NiAl_2O_4$ structure.

The FT-IR spectrum of the pure DR23 dye is shown in Fig. 3d. The band at 1618 with a shoulder at 1637 cm^{-1} is denoted by the carbonyl stretching vibration of the amide functional moiety (C=O was bonded to the N-H bond). N-H angular deformation accompanied by the C(O)-N (amide) stretching. The stretching vibration of amide N-H bond was aligned at 3400-3200 cm^{-1}, and the related bending vibration stood at 1530 cm^{-1}. The peak at C-N stretching vibration revealed at 1380 cm^{-1}. The stretching band of azo groups (-N=N-) has occurred at 1492 cm^{-1}. The symmetric stretching vibrations of SO_3^- moiety ($Ï_s(SO_3^-)$) are shown in peaks 1150/1050 cm^{-1} The band at 1220 cm^{-1} presents the asymmetric stretching vibrations of SO_3^- group ($Ï_{as}(SO_3^-)$). The absorption peaks in the 800-620 cm^{-1} region represent the N-H bond out-of-plane angular deformation of the amide group [47].

In the FT-IR pattern of DR23 dye adsorbed onto nanocomposite (shown in Fig. 3e), the IR absorption pattern is present with tiny and weak peaks. The pronounced changes were observed for sulfonate stretching vibration modes. The ($Ï_{as}(SO_3^-)$) band at 1220 cm^{-1}, is very weak and shifted to

1215 cm^{-1} after dye adsorption on the nanocomposite. The intensity of ($Ï_s(SO_3^-)$) bands at 1150/1050 cm^{-1} is diminished and slightly shifted to 1140/1043 cm^{-1} in the nanocomposite-DR23 spectrum. All these observations confirmed the strong involvement of the sulfonate group in the DR23 adsorption. The absorption bands related to cerium oxide, aluminum oxide and nickel oxide are clearly defined in the range below 600 cm^{-1}, and according to scientific sources, the absorption of metal oxides occurs in this area [46]. According to other analyzes done, the formation of nanocomposite is evident.

SEM and TEM images. Figure 4 shows TEM image of NiAl-NO_3 LDH (a) with a digital photograph (inset); SEM image of CeO_2/NiO/$NiAl_2O_4$ nanocomposite (b) with a digital photograph (inset).

The conventional co-precipitation method for synthesizing LDH compounds either at varied or constant pH yields a vast range of distribution in particle size of LDH plate-like with secondary particle size from several tens of nm to 10 µm. Because the nuclei formed at the beginning of the co-precipitation system had good crystalline growth due to having more opportunity than the nuclei formed at the end [48]. According to Fig. 4a, the co-precipitation method has harvested NiAl-NO3 hexagonal-shaped LDH with several nm to 100 nm in size. The SEM image in Fig. 4b also showed the size of particles estimated to be around 50-70 nm. The morphology of the synthesized nanocomposite is spherical.

DLS experiment was recorded, as shown in Fig. 5. The particle size of CeO_2/NiO/$NiAl_2O_4$ nanocomposite according to the DLS is moderately 71.68 nm. The slight difference in the particle size estimation between TEM and DLS is ascribed to aggregated LDHs.

In the EDX analysis of nanoparticles (Fig. 6), strong signals were observed from the Ni atoms in the nanocomposite at around 7 keV. Elemental mapping results indicate the distribution of elements.

Thermal analysis. Figure 7 shows TG/DTG analysis curves of NiAl-NO_3 LDH under argon gas flow. The thermal decomposition result exhibited two distinct weight loss stages. When the temperature rises from 25 °C to 200 °C, the surface water and interlayer water are removed and weight loss in the form of an endothermic peak is observed in the DTG diagram.

The second endothermic peak happened at a temperature range of 250-500 °C due to the decomposition of LDH

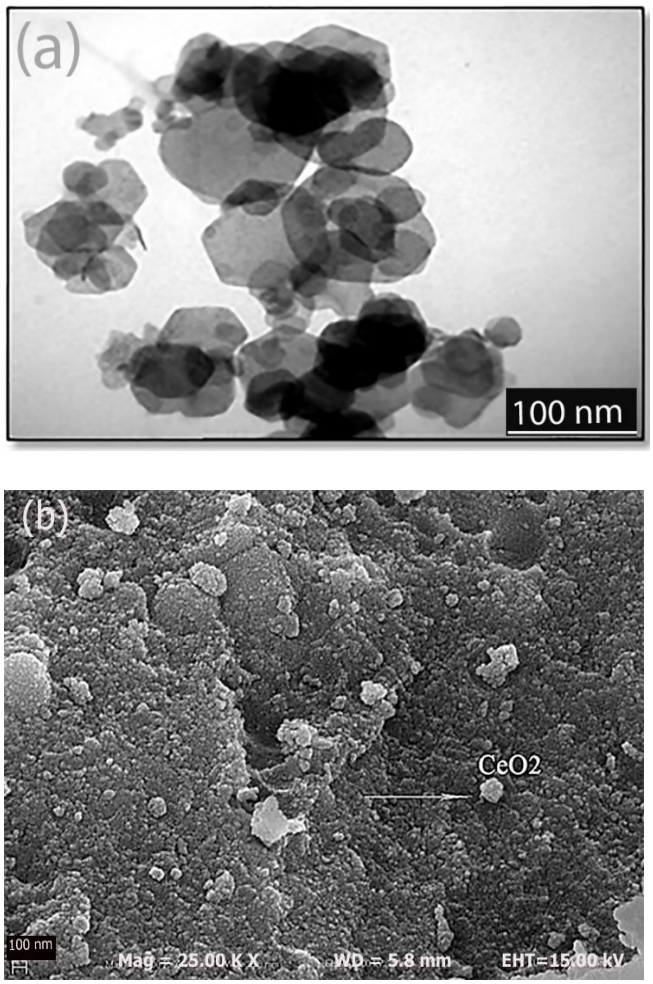

Fig. 4. a) TEM image of the parent NiAl-NO_3 LDH and b) SEM image of nanocomposite.

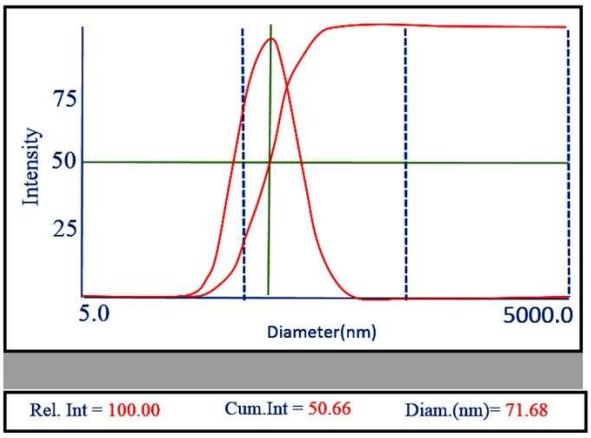

Fig. 5. Dynamic light scattering diagram of CeO_2/NiO/$NiAl_2O_4$ nanocomposite.

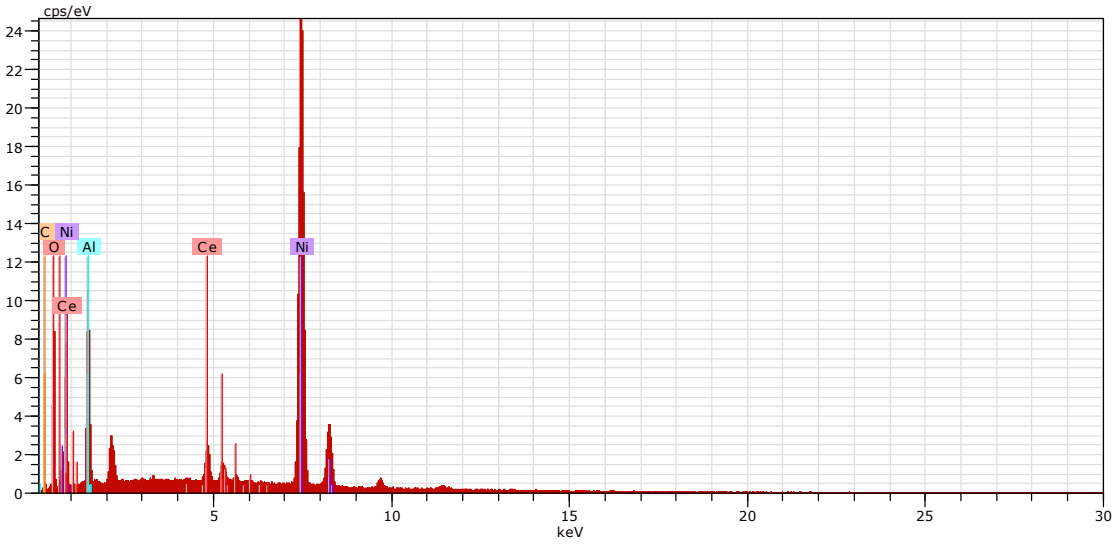

HV:30.0kV Puls th.:15.13kcps

El	AN	Series	unn. C [wt.%]	norm. C [wt.%]	Atom. C [at.%]	Error [wt.%]
Ni	28	K-series	46.86	62.14	39.46	1.2
Al	13	K-series	13.18	17.47	24.14	0.7
O	8	K-series	9.01	11.95	27.84	1.3
Ce	58	L-series	4.68	6.21	1.65	0.2
C	6	K-series	1.68	2.23	6.91	0.5
		Total:	75.41	100.00	100.00	

Fig. 6. EDX analysis of nanoparticles.

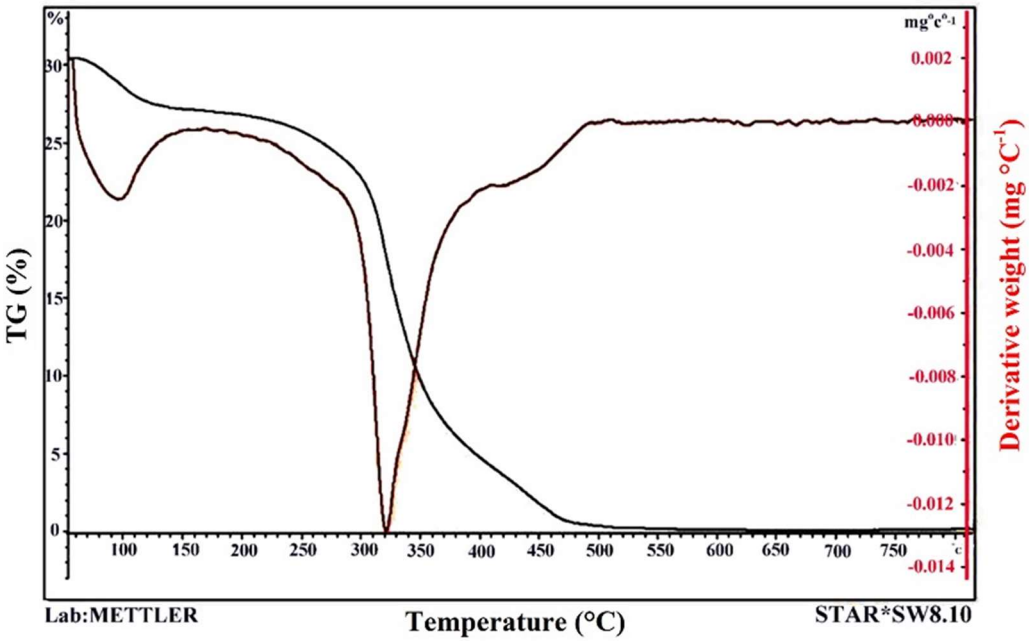

Fig. 7. TG/DTG curves of NiAl-NO_3 LDH.

layered structure by dehydroxylation and losing interlayer anions with a corresponding intense endothermic peak in the DTG curve. Figure 7 shows approximately 30% weight loss of NiAl-NO_3 LDH.

Effect of Operational Parameters on Dye Removal

The adsorption mechanism. The number of active sites, surface charges and functional groups are the factors involved in the absorption process. Control of the solution pH is vital for maximum dye adsorption. The effect of pH as an important factor in the adsorption process was investigated at pH 4-12, with the 24 mg l^{-1} dye solution and 30 mg l^{-1} of nanocomposite in the contact time of 180 min at 293 K. The results of investigating the effect of pH for removal of DR23 by CeO_2/NiO/$NiAl_2O_4$ nanocomposite are shown in Figure 8. As the pH values increase, the removal equilibrium factor (q_e) as well as removal value rate (R%) decresed; therefore, according to these results, pH 4 is selected at 293 K.

It should be noted that the λ_{max} of DR23 lies in the sharply narrow range of 505-506 nm in the UV-Vis absorption region in the blank solutions (without sorbent) of dye at various pH; it has been observed that the λ_{max} dose not affected in the dye solutions. DR23 dye produces sodium ions (Na^+) and sulfonate anions (R-SO_3^-) when dissolving in water. Due to the negative pK_a value of the associated sulfonic acid (pK_a ~ -7), DR23 is negatively charged by maintaining its sulfonate groups even at higher acidic solutions. Therefore, the nanocomposite surface charge is influenced by changing the pH and the adsorption of anionic DR23 dye has been changed. Since hydrotalcite-like materials are precursors of the mixed metallic oxides possessing acidic-basic sites on metal oxides with an effect of predominant basicity, especially those accompanied with Ce, at high acidic solutions, the exposed oxygen atoms (Lewis base sites) of the CeO_2/NiO/$NiAl_2O_4$ nanocomposite are protonated to the (-OH^+) form. Thus, at lower pHs, the surface of the adsorbent is protonated and the electrostatic forces through negatively charged dye and positive adsorbent formed strongly, as shown in Eq. (4):

$$M\text{-}OH^+ + R\text{-}SO_3^- \rightarrow M\text{-}OH^+ \ldots {}^-O_3S\text{-}R \quad (4)$$

In contrast, coordinately unsaturated Al^{3+} and Ce^{4+} are Lewis acid sites in which the adsorption process occurs through a bidentate type system between sulfonate moiety and Al^{3+} or Ce^{4+} cations.

Figure 9 shows the probable adsorption mechanism of DR23 on the nanocomposite. The dye molecules are split in contact with the solvent and released in anionic form. First, a small number of anions are absorbed on the surface of the adsorbent, but most of them leave the surface due to a huge negative potential difference. But because this adsorbent contains cations of cerium and aluminum with empty orbitals ready to receive electrons, it acts like an electrolyte, reduces negative potential, and increases electrostatic absorption.

Unlike increasing the sample pH, the presence of excess OH^- ions in the solution media besides the anionic dye hinders the "a" direction of the suggested mechanism, creating an adsorption competition between them (OH^- and anionic dye) to the adsorbent surface until reaching to equilibrium at moderate pHs [49,50].

At a high basic pH range from 8-12, the adsorption process was slightly increased toward the minimum point of the curve, as depicted in Fig. 8. In addition to the quenching of the "a" pathway of the adsorption process, such observation could be assigned to the very small amount of reconstruction of the LDH structure according to the "memory effect" property in a harsh OH^- environment at 338 K that increases the removal of anionic dye by uptaking the OH^- species between the sheets of the LDH and decreasing the adsorption contest between hydroxide ions and anionic dye on the nanocomposite surface. Also, it is possible that the anionic dye could be inserted between the layers of the LDH through the reconstruction process. This observation may be due to some NiO containing a small amount of Al^{3+} ions that lead to LDH reconstruction at pH = 8-12 at 338 K [41,51]. Notwithstanding, it was not determined the trace of the LDH reconstruction probability by XRD pattern carrying out for the dye adsorbed nanocomposite at pH of 12 at 338 K (not be shown).

Effect of temperature and contact time. To evaluate the influence of different temperatures on dye removal process, DR23 adsorption studies were performed at several temperatures (T = 293-338 K). Therefore, the solutions of DR23 quantity of 24 mg l^{-1} were made and fixed at the optimum pH of 4 by adding a slight amount (not exceeding more than 1% of the total solution volume) of NaOH (0.01 M) aqueous solution. About 100 ml of the described solution was placed into the thermostatic flask and put in an

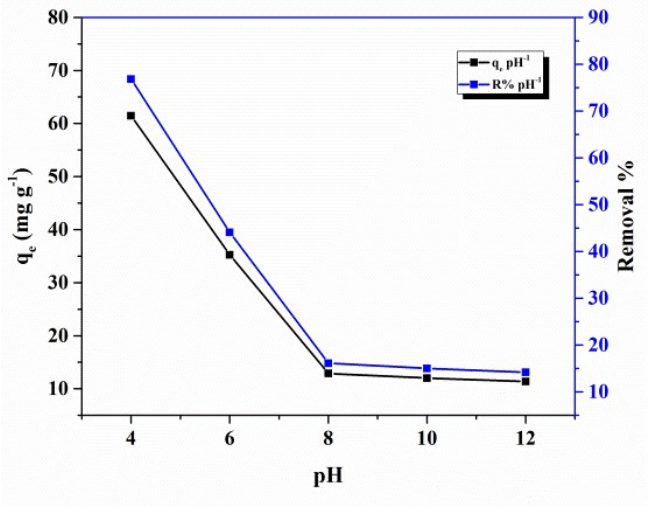

Fig. 8. DR23 adsorption changes at different pHs; [DR23] = 24 mg l^{-1}, T = 293 K, contact time = 180 min and adsorbent dosage = 30 mg l^{-1}.

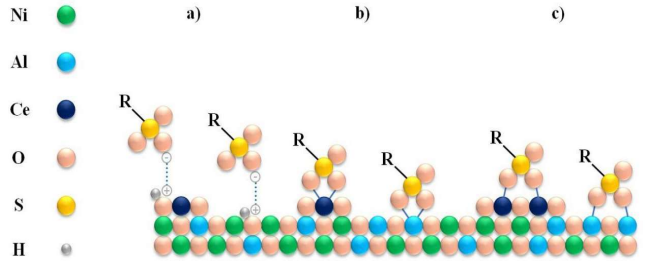

Fig. 9. Mechanism of DR23 adsorption on CeO_2/NiO/$NiAl_2O_4$ surface: (a) electrostatic forces between positively charged nanocomposite and negatively charged dye; (b) and (c) bidentate system between sulfonate group and Al^{3+} or Ce^{4+} cations (the amounts of Ni^{2+} and Al^{3+} have been represented randomly and does not refer to Ni^{2+}/Al^{3+} molar ratio in nanocomposite structure).

oil bath to reach to the isothermal point in the range of 293-338 K. Then, the appropriate amount of adsorbent (30 mg l^{-1} of nanocomposite) was introduced into the vessels. After capping in darkness to eliminate any slight probability of the association of light irradiation in the removal process, the solution was magnetically stirred at the rate of 100 rpm for the appropriate interaction chance. After time intervals of contact, 1 ml of sample solution was drawn out and centrifuged and the supernatant concentration was measured using an UV-Vis spectrophotometer and the removal data, including the adsorption rate, the quantity of adsorbed dye with contact time and R% were shown in Fig. 10a,b,c, respectively. As shown in Fig. 9, by increasing the contact time up to 20 min, the removal rate of the dye is increased until it reaches equilibrium. In which the adsorption amounts of DR23 increased rapidly in the initial 20 min, slowed down and finally attained equilibrium. This was maybe because of the availability of multiple vacant places on the nanocomposite adsorbent available in the beginning time, but then, a narrow slice of the remaining vacant surface of the adsorbed nanocomposite was available for dye removal that was accompanied with the repulsive power between the dye component on the nanocomposite and ones in the solution. So, after passing the initial rapid stage, the adsorption will continue by spending the contact time and lowering the up-taking speed to reach equilibrium.

Moreover, by increasing the temperature, the adsorption capacity (q_t) increases as well. The highest adsorption rate was recorded at 338 K at optimum pH of 4 with 98.63% removal, according to Fig. 10a, c. This observation might be due to the endothermic mechanism of the adsorption and subsequent enhancement in the number of the effective collision between the absorbent and dye adsorbate in the light of the temperature elevation.

Adsorption Kinetics

To study the exact dye removal mechanism, kinetic studies were studied in detail. Checking the dye removal speed is important because it helps to identify and optimize the effective parameters in the dye removal process. Therefore, knowing how fast the dye removal mechanism is done helps significantly design the exact dye removal system [52]. Two equations are used to investigate the rate of removal and dye diffusion; a linear form of Lagergren pseudo-first-order and the linear arrangement of Ho and McKay pseudo-second-order [53], respectively, as follows in Eqs. (5) and (6);

$$\log(q_e - q_t) = \log q_e - (k_1/2.303)t \quad (5)$$

$$\frac{t}{q_t} = \frac{1}{k_2 q_e^2} + \frac{1}{q_e} t \quad (6)$$

where q_e and q_t represent the dosage of adsorbed DR23 per

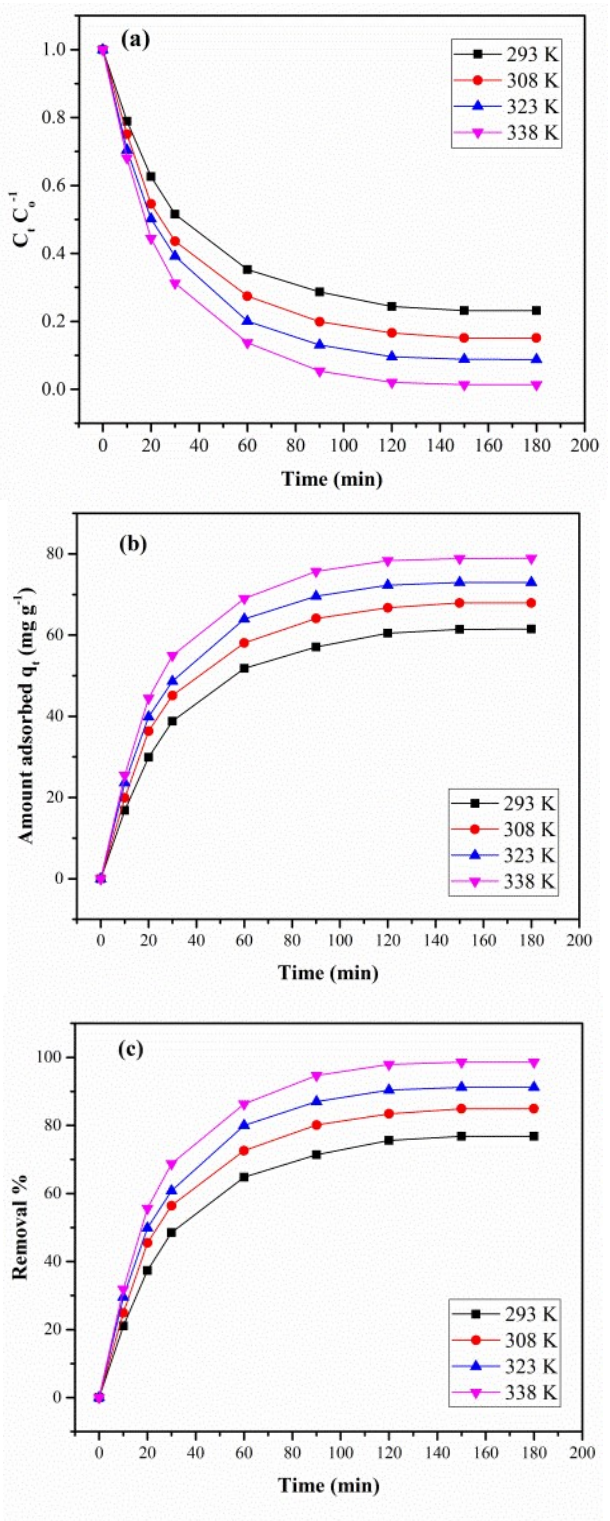

Fig. 10. a) The adsorption rate; b) the amount of adsorbed dye with contact time and c) R%
[DR23] = 24 mg l^{-1}; ads. Dosage = 0.03 g l^{-1}; T = 293-338 K; pH = 4.

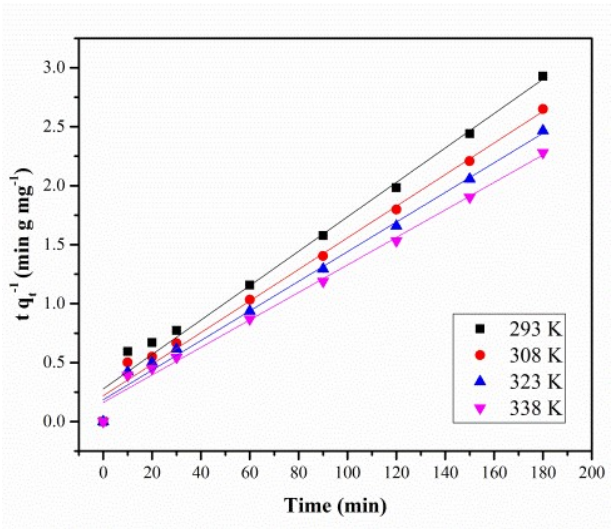

Fig. 11. The pseudo-second-order model graphs for the DR23 adsorption on the nanocomposite.

unit mass of adsorbent (mg g^{-1}) at equilibrium and any other time, respectively, and t (min) is the adsorption time. Also, k_1 (min^{-1}) and k_2 (g mg^{-1} min^{-1}) are the adsorption rate constants of pseudo-first-order and pseudo-second-order models, respectively. The values of k_1 and q_e in the pseudo-first-order model can be obtained from the curve of $\log(q_e - q_t)$ *versus* t. The values of k_2 and q_e in pseudo-second-order model can be obtained from the intercept and slope of the linear plots of $(t\ q_t^{-1})$ against$t$, respectively. The relationship between the predicted data and experimental ones is investigated by the correlation coefficient (R^2) and the closer R^2 values to 1 denote the better agreement. Therefore, the model used in predicting behave well. The linear fitted pseudo-second-order kinetic model plots for the dye adsorption onto the nanocomposite were plotted at different temperatures (293-338 K) and depicted in Fig. 11.

The comparison of the kinetic values and correlation coefficients for the removal of DR23 by CeO_2/NiO/$NiAl_2O_4$ nanocomposite in pseudo-first-order and pseudo-second-order models are shown in Table 3.

The data do not follow pseudo-first-order kinetics but agree with pseudo-second-order models, which examine and is based on the dye removal process throughout the adsorption range [37]. Also, the pseudo-second-order equilibrium rate constant increases while temperature elevates to about 338 K.

Table 3. Kinetic Parameters and Correlation Coefficients (R^2) for the Removal of DR23 (24 mg l^{-1}) by CeO_2/NiO/$NiAl_2O_4$ (0.03 g l^{-1}) Nanocomposite

		Pseudo-first-order model			Pseudo-second-order model		
Temperature (K)	q_e experimental (mg g^{-1})	k_1 (min^{-1}) $\times 10^{-2}$	q_e (mg g^{-1})	R^2	k_2 (g mg^{-1} min^{-1}) $\times 10^{-4}$	q_e (mg g^{-1})	R^2
293	61.4693	4.86	102.8253	0.8559	7.69	68.4931	0.9809
308	67.9386	4.88	106.8563	0.8548	8.21	74.6268	0.9855
323	72.9825	4.81	104.1118	0.9264	8.57	79.3651	0.9881
338	78.9035	5.20	121.7587	0.9108	8.41	85.4700	0.9889

Adsorption Isotherms

Two equations Langmuir and Freundlich equilibrium isotherm models apply to comprehend the adsorption system and the adsorption surface behavior in the dye removal process. The data extracted from these two equations will be very important in interpreting the adsorbent and adsorbed behavior. Depending on which equation the laboratory data best matches, the adsorbent design system will be based on it for further use in the industry [37]. Calculations of laboratory data are performed at four different temperatures using these two equations.

Langmuir isotherm. Langmuir's adsorption theory is obtained using the law of physical adsorption of gas molecules on a solid surface. The surface of an adsorbent is uniform and homogeneous and all sites have the same priority for adsorption. Each location does not absorb more than one molecule, so a monolayer of components will be accommodated on the adsorbent surface. In this experimental model, the surface adsorption is monolayer, so there is no subsequent bonding or spatial barrier between the components in adjacent locations [54]. The Langmuir adsorption isotherm is much better and more common. Because it is possible to optimize it with mathematical equations to generalize to the Yuden bilayer, there is no need for adsorbent concentrations in the equations (unlike Freundlich equations). Therefore, the maximum adsorption capacity q_m is calculated using Langmuir isotherm model and adsorption is assumed to be a monolayer given by the following linear form in Eq. (7):

$$\frac{1}{q_e} = \frac{1}{q_m} + \frac{1}{q_m K_L C_e} \quad (7)$$

in which C_e (mg l^{-1}) is the equilibrium concentration of DR23 in solution, q_e (mg g^{-1}) is the amount of DR23 adsorbed at equilibrium, q_m (mg g^{-1}) and K_L (l mg^{-1}) are the Langmuir constants related to the theoretical maximum monolayer saturation capacity and energy of the adsorption process, respectively. The values of q_m and K_L were calculated from the intercept and slope of the linear plot of q_e^{-1} *vs.* C_e^{-1}.

Freundlich isotherm. The multilayer adsorption isotherm for inhomogeneous surfaces is expressed by the Freundlich isotherm [55]. The following formula calculates the linear form of the Freundlich isotherm (Eq. (8)):

$$\ln q_e = \ln K_F + \frac{1}{n_F} \ln C_e \quad (8)$$

The Friendlich isotherm shows the connection between the amount of dye absorbed per unit mass of adsorbent (q_e) and the concentration of dye in solution at equilibrium (C_e); where K_F (l g^{-1}) and n is the experimental coefficients of the Freundlich equation, which represent the adsorption capacity and intensity, respectively. The coefficient n in the Freundlich equation indicates the degree of heterogeneity of the surface in terms of adsorption sites and its value varies from zero to 1. The closer n is to each other suggests the homogeneity of the adsorption sites and the slight diversity of the surface adsorption sites. Conversely, when n tends to zero, the heterogeneity of adsorption sites increases, indicating a wide range of adsorption sites. The plot of

Table 4. Data on Langmuir and Freundlich Adsorption Isotherms

Temperature (K)	Langmuir isotherm			Freundlich isotherm		
	q_m (mg g^{-1})	K_L (l mg^{-1})	R^2	K_F (m g^{-1})	n_F	R^2
293	161.2903	0.1148	0.8524	20.0447	1.5013	0.8680
308	312.5000	0.0751	0.9827	24.0270	1.2622	0.9857
323	250.0000	0.1914	0.9826	41.7157	1.3831	0.9876
338	588.2353	0.4595	0.9984	205.6840	1.1431	0.9990

$\ln q_e$ *vs.* $\ln C_e$, with the slope of n_F^{-1} is a straight line confirming the Freundlich isotherm model [56]. The calculated constants of Langmuir and Freundlich isotherms and related correlation coefficient (R^2) were given in Table 4. By fitting the DR23 adsorption data to the as-mentioned isotherms at equilibrium, the results indicate that the data show better agreement with the Friendlich model than Langmuir, accounting for Fig. 12.

Adsorption mechanisms of anionic materials are similar [57], aromatic organic acids [58], organic compounds [59] and anionic surfactants [60] onto activated carbon cloth.

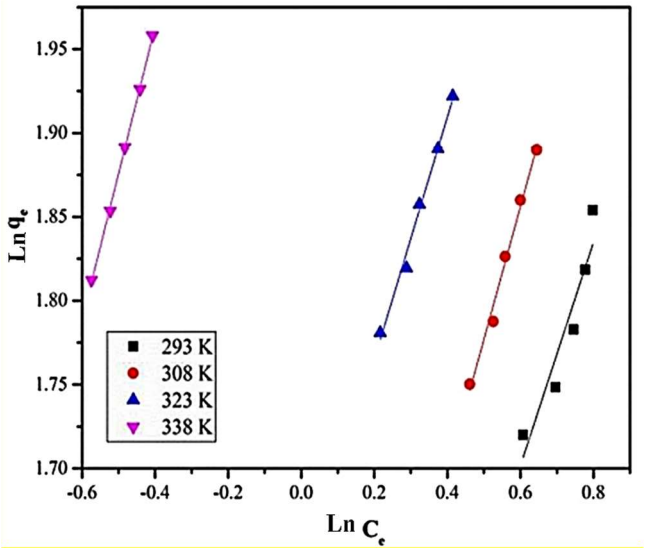

Fig. 12. Freundlich model for DR23 adsorption at temperature ranges of 293-338 K.

Thermodynamic Studies

By examining the changes in the amount of adsorption in terms of temperature, we can comment on the nature of the reaction (heat or exothermicity). It is calculated from the slope of the curves. It can also be found that physical adsorption on a solid bed takes place by a chemical or physical bond. The lower the adsorption process at a lower temperature, the more economically viable it is the value of $\Delta H°$ also indicates the degree of the tendency of the adsorbent to be absorbed. From ($\Delta S°$) we can see the increase or decrease of entropy. The standard free energy changes ($\Delta G°$) can be obtained using the Eq. (9) at different temperatures (298 to 338 K) [61,62]:

$$\Delta G° = -RT \ln K_L \quad (9)$$

where R (8.314 J mol^{-1} K^{-1}) is the universal gas constant; T (K) stands for the absolute temperature of the solution; and K_L (l mg^{-1}) represents the Langmuir isotherm constant.

The standard enthalpy change ($\Delta H°$) and the standard entropy change ($\Delta S°$) were obtained using the following formula shown in Eq. (10):

$$\ln K_L = \frac{\Delta S°}{R} - \frac{\Delta H°}{RT} \quad (10)$$

In a Van't Hoff plot of $\ln K_L$ against T^{-1} is a straight line with $\Delta H°$ and $\Delta S°$ as slope and intercept, respectively. Thermodynamic variables of dye adsorption on nanocomposite were calculated and the obtained data were tabulated in Table 5.

The negative value obtained for standard free energy changes ($\Delta G°$) confirms the automatic adsorption reaction. When the temperature decreased from 298 to 338 K, $\Delta G°$ was

Table 5. Thermodynamic Parameter of Gibbs Free Energy, Enthalpy, and Entropy for the DR23 Adsorption by the Nanocomposite

Temperature (K)	$\ln K_L$	$\Delta G°$ (kJ mol^{-1})	$\Delta H°$ (kJ mol^{-1})	$\Delta S°$ (J mol^{-1} K^{-1})
298	2.39	-5.920	61345.68	223.85
308	2.92	-7.475		
323	3.53	-9.486		
338	5.47	-1.5362		

increased from -5.921 kJ mol^{-1} to -15.363 kJ mol^{-1}, and the adsorption capacity increased with elevating the temperature. The endothermic nature of the adsorption reaction is confirmed by the positive value of $\Delta H°$, which agrees with the isotherm. Also it is evident from Table 5 that another thermodynamic parameter ($\Delta S°$), has a positive value and this represents the cohesion of the dye on the adsorbent.

Regeneration Experiments

The recyclability potential of nanocomposite used in DR3 removal was tried by the several cycles of adsorption using the same adsorbent. Desorption of dye from regenerated adsorbent after its revival is one of the important economic and environmental issues. These experiments have been done on saturated dye adsorbed nanocomposite under optimized conditions. According to the solution pH and temperature influences the adsorption process (shown in Figs. 7 and 9b), the least uptaking occurred at a pH value of 8 at room temperature. Accordingly, dye desorption of 89% was achieved in an aqueous solution of high OH^- concentration at pH 8 under vigorous magnetically shaking at room temperature for 2 h. High pH value accompanied by vigorously stirring or shaking action cause replacing the adsorbed dye molecules on the external space of the adsorbent with numerous dense amounts of OH^- exist in the solution environment. Approximately 10% loss of the adsorbent capacity may be due to the close junction between dye and nanocomposite or secondly implementing dye component in the inter-lamellar space of the probable slight LDH reconstruction from the nanocomposite at high pH condition according to the memory effect property due to the probable existence of trace Al^{3+} ion inside the NiO phase [63]. Adsorption results of DR23 removal by the regenerated nanocomposite in 5 stages for regeneration and re-usage cycles are shown in Fig. 13.

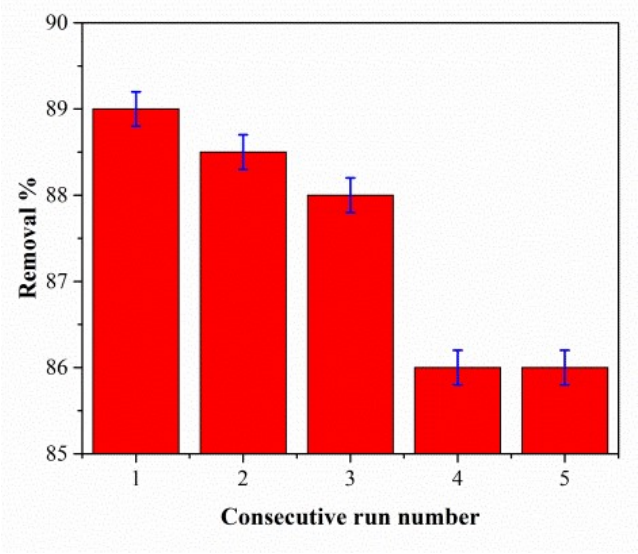

Fig. 13. Comparison of nanocomposite reusability within the five consecutive regenerated materials. (Adsorption condition: pH = 4 and Temp. = 338 K; desorption condition: pH = 8 and Temp. = 293 K).

In Table 6, the adsorption methods that have been used so far to remove the DR23 are reported along with the related parameters. Nano adsorbents contain a high capacity to remove contaminants by adsorption, have huge potential for the remediation of pollutants from wastewater and open the field for environmental application. The nanocomposite synthesized in this research work has used cheap and available materials (mineral materials), reducing the production cost. The proposed nanocomposite has obtained a high adsorption capacity (588.24 mg g^{-1}) compared with the

Table 6. DR23 Removal Using Different Adsorbents

a) Nano sized adsorbents:

Adsorbent	pH	Temperature (°C)	q_m (mg g^{-1})	Ref.
powdered tourmaline	3	25	153	[64]
CS-g-PNEANI copolymer	2	25	112	[65]
GO	3	20	15.3	[16]
Activated carbon in a rotating packed bed (RPB)	-	-	8.35	[66]
ZFN-CTAB	2	25	26.1	[67]
Magnetic multi-walled carbon nanotubes-Fe_3C nanocomposite (MMWCNTs-ICN)	3.7	30	172.4	[68]
Polyaminoimide homopolymer (PAIHP)	2	25	5555	[69]
TiO_2	<4.5	-	2.2-35.2	[70]
CeO_2/NiO/$NiAl_2O_4$	4	65	588.24	This work

b) Macro sized adsorbents:

Adsorbent	pH	Temperature (°C)	q_m (mg g^{-1})	Ref.
Orange peel	2	25	10.72	[71,72]
Magnetic (barium ferrite)-chitosan beads	4	25	1250	[73]
Uncaria gambir (gambir)	2	30	26.67	[74]
Magnetic corn stalk	3	25	27-52	[75]
Cationized wood sawdust	6.5	30	65.8	[76]
Untreated and activated rice husk by citric acid	-	25	2.41 4.35	[77]
Rhizophora apiculata bark	<7	30	21.6	[78]

Abbreviations: CS-g-PNEANI; chitosan-g-poly(N-ethylaniline), GO; graphene oxide, ZFN-CTAB; zinc ferrite nanoparticle-cetyl trimethylammonium bromide.

cited works in Table 6. The adsorbent's excellent adsorption capacity was demonstrated by high removal percentage (more than 98%) towards the DR23 in experimental runs. In addition, the reusability was also performed up to three cycles with 89, 85, and 88% efficiency for DR23.

CONCLUSIONS

A novel nanocomposite (CeO_2/NiO/$NiAl_2O_4$) adsorbent for removing DR23 from aqueous solutions is investigated. This adsorbent removes anionic DR23 dye molecules with the maximum adsorption capacity of 588.24 mg g^{-1} at an optimum pH value of 4 at 65 °C. The data obtained in the laboratory were modeled using Langmuir and Freundlich isotherms and it is observed that the adsorption mechanism accounts better for the Freundlich model (R^2 is in the range of 0.8680-0.9990). The adsorption kinetic trend is the pseudo-second-order model. According to the thermodynamic variable of dye adsorption performance on nanocomposite, the positive amount of $\Delta H°$ reveals the endothermic mechanism of the removal; the positive $\Delta S°$ represents the cohesion of the dye on the adsorbent, and the

negative values for $\Delta G°$ prove spontaneous characteristic of the adsorption and this represents the integrity of adsorbent in adsorption procedure. Dye saturated nanocomposite was regenerated at pH value of 8. The results showed that the CeO_2/NiO/$NiAl_2O_4$ adsorbent is a suitable candidate for removing DR23 dye from textile wastewater due to its fast and efficient dye removal mechanism and good recyclability.

ACKNOWLEDGMENTS

This work is supported by Food and Drug Safety Research Center, Tabriz University of Medical Science, Tabriz, Iran, with grant number 61243.

REFERENCES

[1] M.A. Nazir, M.A. Bashir, T. Najam, M.S. Javed, S. Suleman, S. Hussain, O.P. Kumar, S.S.A. Shah, A. ur Rehman, Microchem. J. 164 (2021) 105973.
[2] G. Yin, Z. Sun, Y. Gao, S. Xu, Microchem. J. 166 (2021) 106190.
[3] F. Deniz, E.T. Ersanli, Microchem. J. 128 (2016) 312.
[4] M. Daoud, O. Benturki, P. Girods, A. Donnot, S. Microchem. J. 148 (2019) 493.
[5] S. Xing, Z. Zhou, Z. Ma, Y. Wu, Appl. Catal. B 107 (2011) 386.
[6] H. Zollinger, Color Chemistry: Syntheses, Properties, and Applications of Organic Dyes and Pigments, John Wiley & Sons, 2003.
[7] U. Balçık, D.S. Microchem. J. 155 (2020) 104712.
[8] C. Bauer, P. Jacques, A. Chem. Phys. Lett. 307 (1999) 397.
[9] R.L. Singh, P.K. Singh, R.P. Singh, Int. Biodeterior. Biodegradation 104 (2015) 21.
[10] M. Bhaskar, A. Gnanamani, R.J. Ganeshjeevan, R. Chandrasekar, S. Sadulla, G. Radhakrishnan, J. Chromatogr. A 1018 (2003) 117.
[11] S. Song, H. Ying, Z. He, J. Chen, Chemosphere 66 (2007) 1782.
[12] V. Venkateswaran, V. Priya, P. Balasubramaniyam, Chem. Sci. Trans. 2 (2013) 771.
[13] J. Shore, Advances in Direct Dyes, 1996.
[14] I. Pavlovic, C. Barriga, M. Hermosín, J. Cornejo, M. Ulibarri, Appl. Clay Sci. 30 (2005) 125.
[15] L.P. Cardoso, R. Celis, J. Cornejo, J.B. Valim, J. Agric. Food Chem. 54 (2006) 5968.
[16] G. Crini, Bioresour. Technol. 97 (2006) 1061.
[17] T. Robinson, G. McMullan, R. Marchant, P. Nigam, Bioresour. Technol. 77 (2001) 247.
[18] E. Ayranci, O. Duman, J. Sep. Sci. 44 (2009) 3735.
[19] E. Ayranci, O. Duman, Chem. Eng. J. 156 (2010) 70.
[20] O. Duman, S. Tunc, T.G. Micropor. Mesopor. Mat. 210 (2015) 176.
[21] O. Duman, S. Tunç, T.G. Polat, Appl. Clay Sci. 109 (2015) 22.
[22] O. Duman, S. Tunç, T.G. Polat, B.K. Bozoğlan, Carbohydr. Polym. 147 (2016) 79.
[23] O. Duman, S. Tunç, B.K. Bozoğlan, T.G.J. Alloys Compd. 687 (2016) 370.
[24] F. Cavani, F. Trifirò, A. Vaccari, Catal. Today 11 (1991) 173.
[25] X. Duan, D.G. Evans, 119 (2006) Springer Science & Business Media.
[26] F. Li, X. Duan, 2006, Springer, 193.
[27] R. Marangoni, M. Bouhent, C. Taviot-Guého, F. Wypych, F. Leroux, J. Colloid Interface Sci. 333 (2009) 120.
[28] Y. Li, B. Gao, T. Wu, B. Wang, X. Li, J. Hazard. Mater. 164 (2009) 1098.
[29] M. Bouraada, F. Belhalfaoui, M. Ouali, L.C. De Menorval, J. Hazard. Mater. 163 (2009) 463.
[30] X. Wang, P. Wu, Y. Lu, Z. Huang, N. Zhu, C. Lin, Z. Dang, Sep. Purif. Technol. 132 (2014) 195.
[31] H. Xiao, Z. Ai, L. Zhang, J. Phys. Chem. 113 (2009) 16625.
[32] J. Wu, J. Wang, Y. Du, H. Li, X. Jia, J. Nanopart. Res. 18 (2016) 1.
[33] N.a.M. Tomić, Z.D. Dohčević-Mitrović, N.M. Paunović, D.a.Z. Mijin, N.D. Radić, B.k.V. Grbić, S.M. Aškrabić, B.M. Babić, D.V. Bajuk-Bogdanović, Langmuir 30 (2014) 11582.
[34] J. Fang, X. Bi, D. Si, Z. Jiang, W. Huang, Appl. Surf. Sci. 253 (2007) 8952.
[35] J.S., Valente, F. Tzompantzi, J. Prince, Appl. Catal. B 102 (2011) 276.
[36] A. Chaparadza, J.M. Hossenlopp, Removal of 2,4-dichlorophenoxyacetic acid by calcined Zn–Al–Zr layered double hydroxide. Appl. Surf. Sci. 363 (2011) 92.
[37] S. Nethaji, A. Sivasamy, G. Thennarasu, S. Saravanan,

J. Hazard. Mater. 181 (2010) 271.
[38] A. Khenifi, Z. Derriche, C. Mousty, V. Prévot, C. Forano, Appl. Clay Sci. 47 (2010) 362.
[39] J. Olanrewaju, B. Newalkar, C. Mancino, S. Komarneni, Mater. Lett. 45 (2000) 307.
[40] T. Zhang, Q. Li, H. Xiao, Z. Mei, H. Lu, Y. Zhou, Appl. Clay Sci. 72 (2013) 117.
[41] F. Kovanda, T. Rojka, P. Bezdička, K. Jirátová, L. Obalová, K. Pacultová, Z. Bastl, T. Grygar, J. Solid State Chem. 182 (2009) 27.
[42] S. Mandal, D. Tichit, D.A. Lerner, N. Langmuir 25 (2009) 10980.
[43] M.J. Hernandez-Moreno, M.A. Ulibarri, J. Rendon, C.J. Serna, Phys. Chem. Miner. 12 (1985) 34.
[44] V. Rives, S. Kannan, Phys. Chem. Miner. 10 (2000) 489.
[45] M.K. Titulaer, J.B.H. Jansen, J.W. Geus, Clays Clay Miner. 42 (1994) 249.
[46] N.T. McDevitt, W.L. Baun, Spectrochim. Acta 20 (1964) 799.
[47] R.M. Silverstein, F.X. Webster, D.J. Kiemle, D.L. Bryce, John Wiley & Sons, 2014
[48] Y. Zhao, F. Li, R. Zhang, D.G. Evans, X. Duan, Chem. Mater. 14 (2002) 4286.
[49] C. Namasivayam, D. Kavitha, Dyes Pigm. 54 (2002) 47.
[50] Y. Fu, T. Viraraghavan, Adv. Environ. Res. 7 (2002) 239.
[51] N. Leont'eva, S. Cherepanova, V. Drozdov, J. Struct. Chem. 55 (2014) 1326.
[52] C. Quintelas, E. Sousa, F. Silva, S. Neto, T. Tavares, Process Biochemistry 41 (2006) 2087.
[53] Y.S. Ho, G. McKay, Pseudo-second order model for sorption processes. Process Biochemistry 34 (1999) 451.
[54] I. Langmuir, J. Am. Chem. Soc. 3 (1917) 1848.
[55] H. Freundlich, J. Phys. Chem. 57 (1906) 470.
[56] E.R. Alley, Water Quality Control Handbook.: McGraw-Hill, New York, 2007.
[57] O. Duman, E. Ayranci, J. Hazard. Mater. 120 (2005) 173.
[58] E. Ayranci, O. Duman, J. Hazard. Mater. 136 (2006) 542.
[59] O. Duman, E. Ayranci, J. Sep. Sci. 41 (2006) 3673.
[60] E. Ayranci, O. Duman, J. Hazard. Mater. 148 (2007) 75.
[61] A. Rahmani, H.Z. Mousavi, M. Fazli, Desalination 253 (2010) 94.
[62] M.A. Ahmad, R. Alrozi, Chem. Eng. J. 171 (2011) 510.
[63] F. Trifiro, A. Vaccari, O. Clause, Catal. Today. 21 (1994) 185.
[64] N. Liu, H. Wang, C.H. Weng, C.C. Hwang, Arab. J. Chem. 11 (2018) 1281.
[65] M. Abbasian, M. Jaymand, P. Niroomand, A. Farnoudian-Habibi, S.G. Karaj-Abad, Int. J. Biol. Macromol. 95 (2017) 393.
[66] A. Kundu, L. Shakira Hassan, G. Redzwan, D. Robinson, M. Ali Hashim, B. SenGupta, Desalination and Water Treat., 57 (2016) 13518.
[67] N.M. Mahmoodi, J. Abdi, D. Bastani, J. Environ. Health Sci. 12 (2014) 96.
[68] W. Konicki, I. Pełech, E. Mijowska, I. Jasińska, Chem. Eng. J. 210 (2012) 87.
[69] N.M. Mahmoodi, F. Najafi, S. Khorramfar, F. Amini, M. Arami, J. Hazard. Mater. 198 (2011) 87.
[70] P.J. Holliman, B. Vaca Velasco, I. Butler, M. Wijdekop, D.A. Worsley, Int. J. Photoenergy, 2008.
[71] M. Arami, N.Y. Limaee, N.M. Mahmoodi, N.S. Tabrizi, J. Colloid Interface Sci. 288 (2005) 371.
[72] F.D. Ardejani, K. Badii, N.Y. Limaee, N. Mahmoodi, M. Arami, S. Shafaei, A. Mirhabibi, Dyes Pigm. 73 (2007) 178.
[73] S.H. Sanlier, G. Ak, H. Yilmaz, G. Ozbakir, O. Cagliyan, Prep. Biochem. Biotechnol. 43 (2013) 163.
[74] A. Achmad, J. Kassim, T.K. Suan, R.C. Amat, T.L. Seey, J. Phys. Sci. 23 (2012) 1.
[75] M. Fathi, A. Asfaram, A. Farhangi, Spectrochim. Acta A: Mol. Biomol. Spectrosc. 135 (2015) 364.
[76] A. Hebeish, M. Ramadan, E. Abdel-Halim, A. Abo-Okeil, Clean. Technol. Environ. Policy 13 (2011) 713.
[77] O. Abdelwahab, A. El Nemr, A. El Sikaily, A. Khaled, Egypt. J. Aquat. Res. 31 (2005) 1.
[78] L.S. Tan, K. Jain, C. Jases, J. Appl. Sci. Environ. Sanit. Sby. 5 (2010) 283.